



Core-shell LaPO₄/g-C₃N₄ nanowires for highly active and selective CO₂ reduction



Mengli Li^b, Lingxia Zhang^{a,*}, Xiangqian Fan^a, Meiyong Wu^a, Min Wang^a, Ruolin Cheng^a, Linlin Zhang^a, Heliang Yao^a, Jianlin Shi^{a,c,*}

^a State Key Laboratory of High Performance Ceramics and Superfine Microstructure, Shanghai Institute of Ceramics, Chinese Academy of Sciences, 1295 Ding-Xi Road, Shanghai 200050, PR China

^b School of Biology and Chemical Engineering, Jiaxing University, Jiaxing, Zhejiang 314001, PR China

^c Jiangsu National Synergetic Innovation Center for Advanced Materials (SICAM), PR China

ARTICLE INFO

Article history:

Received 13 June 2016

Received in revised form 25 August 2016

Accepted 1 September 2016

Available online 1 September 2016

Keywords:

CO₂ photoreduction

Core-shell nanowire

Heterostructure

LaPO₄

Graphite carbon nitride

ABSTRACT

We have synthesized a series of LaPO₄/g-C₃N₄ core-shell nanowires via an *in-situ* hydrothermal growth of LaPO₄ nanorods in tubular g-C₃N₄ and investigated their photocatalytic activity in CO₂ reduction. It was found that in the synthesized core-shell structure, the outer g-C₃N₄ nano-shells coated on the LaPO₄ nanorod cores resulted in the enhanced light absorption and charge carrier separation/transfer ability, thus improved the room temperature photocatalytic performance of the nanocomposites in CO₂ photocatalytic reduction compared with the g-C₃N₄ and LaPO₄ individuals. A maximum CO yield of 0.433 μmol has been obtained from CO₂ reduction within 1 h irradiation on 30 mg nanocomposite photocatalyst under the absence of any noble metal. Finally, a possible mechanism, which is featured with LaPO₄ activation due to significantly promoted separation/transfer of photo-generated charge carriers, was proposed. The encouraging performance in CO₂ photoreduction demonstrates that this novel nanocomposite will be a prospective material in environmental protection and energy conversion.

© 2016 Published by Elsevier B.V.

1. Introduction

Semiconductor-based photocatalysis is considered as one of the most promising technologies to solve the energy shortage and air pollution problems caused by fossil fuel consumption [1,2]. Photocatalysts with high efficiency and excellent stability have been actively pursued, and great numbers of attractive visible-light-driven photocatalysts have been explored [3,4]. Recently, graphitic carbon nitride (g-C₃N₄) with a bandgap of ~2.7 eV as a cost-effective and sustainable semiconductor made up of only carbon and nitrogen has attracted increasing attention since the first pioneering work by Wang et al. in 2009 [5], due to its appealing electronic structure, excellent chemical and thermal stability, easy availability and environmental friendliness [6]. Fortunately, g-C₃N₄ also demonstrates promising photocatalytic performance for CO₂ reduction [7–9]. For the sake of enhanced photocatalytic effi-

ciency of g-C₃N₄, a number of strategies such as doping [10–12], metal deposition [13], texture engineering [14–17], copolymerization [18,19] and so on, have been developed. Among them, constructing g-C₃N₄-based nanostructures and nanocomposites by coupling with other semiconductors will enable the substantial alternations/modifications of electronic band structure and the construction of favorable interface heterostructure, thus enhancing the photocatalysts' efficiency [3,20–23]. To ensure the effective separation/transfer and high reactivity of charge carriers, close bonding between hetero-components is necessary.

The photocatalytic activity for hydrogen evolution from water splitting of several lanthanum-based compounds has been confirmed [24,25]. Besides, alkaline lanthanum ions have been recognized as active sites for CO₂ adsorption [26]. LaPO₄, a typical member of the rare earth phosphate family, was proved to be an effective photocatalyst for CO₂ reduction, but its high photocatalytic activity could only be activated by high-pressure Hg lamp because of its relatively wide bandgap and poor sensitivity to visible light [27]. For years, researchers have mainly focused on the photoluminescence of LaPO₄ [28], and its photocatalytic activity has been rarely reported.

Nanocomposite catalysts have been extensively investigated for enhanced catalytic performances, which, however, are generally

* Corresponding authors at: State Key Laboratory of High Performance Ceramics and Superfine Microstructure, Shanghai Institute of Ceramics, Chinese Academy of Sciences, 1295 Ding-Xi Road, Shanghai 200050, PR China.

E-mail addresses: zhlingxia@mail.sic.ac.cn (L. Zhang), jlshi@mail.sic.ac.cn (J. Shi).

in the forms of multi-particulate or particles-on-nanosheet junctions. Encouraged by the reports on individual g-C₃N₄ and LaPO₄, herein, a novel 1D core-shell LaPO₄/g-C₃N₄ (denoted as La/tCN-*x*, where *x* represents the dosage of tubular g-C₃N₄ in milligram) nanocomposites have been designed and synthesized via a facile hydrothermal method for the first time, which demonstrated high efficiency and stability for photoreduction of CO₂ under simulated sunlight (Xe-lamp) irradiation. Furthermore, this kind of nanocomposites can largely overcome the drawbacks of the corresponding individual components and show much enhanced charge separation efficiency, based on the synergetic catalytic effect between the components [29]. Possible mechanism toward the photocatalysis process has been proposed and discussed in detail. Notably, this work offers a handy and green strategy to achieve enhanced solar photocatalytic activity and provides new insight for the design and development of other high-performance nanocomposite photocatalysts.

2. Experimental

2.1. Synthesis procedure

All the chemicals are analytical grade and used as received without any further purification. Melamine (C₃H₆N₆) and acetone were purchased from Sinopharm Chemical Reagent Co., Ltd.; La(NO₃)₃·6H₂O, nitric acid and (NH₄)₂HPO₄ were all purchased from Aladdin Chemical Reagent, Ltd.; Na₂SO₄, ethylene glycol were both purchased from TCI Co., Ltd.

The tubular g-C₃N₄ was synthesized by a modified chemical method [29]. In detail, 1 g melamine was dissolved in ethylene glycol and stirred for 2 h at ambient temperature to make a saturated solution. 60 mL of 0.1 M nitric acid aqueous solution was added dropwise into 30 mL of the as-prepared melamine solution under vigorous stirring. The generated white precipitation was washing by ethanol and collected by centrifuging for several times. The product was then dried at 60 °C until the ethanol was evaporated completely and annealed at 450 °C in an alumina crucible with a cover for 2 h with a ramp of 10 °C min⁻¹. The crucible was then cooled to room temperature naturally. Subsequently, a thermal post-treatment at 550 °C was executed in air at a heating rate of 10 °C min⁻¹. The obtained tubular g-C₃N₄ was denoted as tCN.

The core-shell structured nanocomposites were prepared as follows: 0.866 g La(NO₃)₃·6H₂O and 0.264 g (NH₄)₂HPO₄ were dissolved in 30 mL distilled water under stirring, respectively. An appropriate amount of tCN was then ultrasonicated in the La(NO₃)₃ solution for 10 min. Then, (NH₄)₂HPO₄ solution was added into the mixture solution with tCN and La(NO₃)₃ under vigorous stirring. One hour later, the mixture was transferred into a 100 mL Teflon-lined autoclave and kept at 160 °C for 20 h in an oven. The resulting samples were washed several times with deionized water, lyophilized overnight, and denoted as La/tCN-*x*, where *x* represents the dosage of tubular g-C₃N₄ in milligram. The detailed contents of g-C₃N₄ in La/tCN-*x* was determined on VARIO EL CUBE microanalyzer and shown in Table S1. LaPO₄ nanorods were synthesized by the same method without adding tCN.

2.2. Characterization

To study the crystallographic phase of the as-prepared catalysts, X-ray diffraction patterns (XRD) were recorded by a Rigaku D/Max 2200PC X-ray diffractometer with Cu Kα (λ = 1.5406 Å) irradiation operating at 40 kV and 40 mA. The scanning rate is 4°/min. Images of transmission electron microscopy (TEM), and high-resolution transmission electron microscopy (HRTEM) were obtained by JEOL JEM-2100F transmission electron microscope (FE-TEM) equipped

with a field emission source at an accelerating voltage of 200 kV. Field emission scanning electron microscopy (FE-SEM) images were obtained using a Hitachi S-4800 field emission scanning electron microscope. X-ray photoelectron spectroscopy (XPS) measurements were carried out on a Thermal Scientific ESCALAB 250 sepectrometer using monochromated Al Kα X-ray as a radiation at 250 W. All the binding energies were calibrated by setting the contaminant carbon (C 1s) to 284.6 eV as reference. Elemental analysis (C, N) was taken on VARIO EL CUBE microanalyzer. Ultraviolet visible (UV-vis) diffuse reflection spectra were recorded in the range of 200–800 nm on a spectrophotometer (Hitachi UV-3101, Shimadzu) using BaSO₄ as a reflectance standard material. Ambient room-temperature photoluminescence (PL) test was operated on a Hitachi F-4500 fluorescence spectrophotometer. Fourier transform infrared (FTIR) spectra were recorded on a Nicolet iZ10 FTIR apparatus at a resolution of 4 cm⁻¹. N₂ adsorption-desorption was conducted on Micromeritics Tristar 2000 instrument and the specific surface area and pore size distribution were calculated by the Brunauer-Emmett-Teller (BET) and the Barret-Hoyner-Halenda (BJH) method, respectively.

2.3. Electrochemical measurements

Electrochemical measurements were carried in a quartzose beaker and on a CHI 660A electrochemical workstation (Shanghai Chenhua Instrument, Inc.) with a standard three-electrode mode. Fluorine-doped Tin Oxide (FTO) coated with photocatalysts served as a working electrode, while a platinum foil as the counter electrode, and the Ag/AgCl electrode as the reference electrode, with 0.2 M Na₂SO₄ aqueous solution as electrolyte solution. For working electrodes, 20 mg of photocatalyst and 40 mg iodine were dispersed in 25 mL acetone to form a homogeneous liquid, and then, the photocatalysts were deposited onto the FTO conductive glasses with an area of 1 cm² by an electrophoretic deposition method. After being stored for 2 h at 150 °C, a homogeneous film can be obtained. A Pt wire and an Ag/AgCl electrode were also used as the counter and reference electrodes for the Mott-Schottky test.

2.4. Photocatalytic activity evaluation

CO₂ photocatalytic reduction was typically conducted in an air-tight circulation system in a reactor (volume: 500 mL) with an optical quartz window at the top which was purchased from PerfectLight Company (China, Beijing). To remove possible organic adsorbates, all the prepared samples were treated at 200 °C in air for 3 h prior to the photocatalytic measurement. In a typical process, 30 mg of the sample was uniformly dispersed on a porous quartzose plate with the area fixed at 2.5 cm × 2.5 cm 80 kPa high purity CO₂ (99.99%) gas, monitored by a mass flow controller, was led to pass through a water bubbler to generate a mixture of CO₂ and water vapor. A 300 W Xenon-arc lamp (Aulight CEL-HX, Beijing) was used as the light source. The temperature of the reactor was controlled at 25 °C through cooling water circulation. The carbonous products were analyzed by a gas chromatograph (GC-2060, Fuli Corp., China) with a flame ionization detector (FID) equipped with a 5A molecular column and a TDX-01 packed column. While the evolved H₂ and O₂ gases were analyzed by gas chromatography (GC7900, Techcomp) equipped with a thermal conductive detector (TCD) and a 5A molecular sieve column. The products were quantized based on the external standard with a calibration curve. During the test, 1 mL of the gaseous product was periodically sampled from the glass chamber at a given time intervals (1 h) to detect the possible products such as H₂, O₂, CO and/or other carbon-based gases. CO can be detected by installing a methanizer, using N₂ as carrier gas. In the photostability measurement, the photocatalysts were heated at 150 °C for another 2 h to eliminate CO or/and other pos-

sible physically adsorbed products. Then, the reactor was purged by high purity N_2 for several times, followed by the mixture of CO_2 and water vapor in each run.

3. Results and discussion

3.1. Characterization of the as-prepared samples

The morphologies of tCN, $LaPO_4$ nanorods, and the La/tCN-200 nanocomposite were observed using a field-emission scanning electron microscope (FE-SEM) and a transmission electron microscope (TEM). As can be seen in Fig. 1a, the as-prepared $LaPO_4$ presents a well-defined nanorod morphology, and the composite sample La/tCN-200 inherits the nanorod morphology of $LaPO_4$ (Fig. 1b). TEM and high-resolution TEM (HRTEM) observation further confirm the homogenous 1D structure of the components and composites (Fig. 1c–f). The tubular-like $g-C_3N_4$ constructed by treating melamine with HNO_3 in the presence of ethylene glycol can be seen clearly in Fig. 1c, though its layered structure has become less ordered and/or its dimension has been reduced in comparison with conventional $g-C_3N_4$, as demonstrated in Fig. S1. In Fig. 1f, it is interesting to find two sets of lattice fringes in La/tCN nanocomposites. The lattice spacing of 0.610 nm and 0.326 nm presented in the picture corresponds to the (100) lattice plane of $LaPO_4$ and (002) lattice plane of tubular-like $g-C_3N_4$, respectively [30–34]. The lattices between the white and yellow lines belong to tCN, while that between white lines corresponds to $LaPO_4$. It seems that two (002) lattice planes of tCN and one (100) lattice plane of $LaPO_4$ share the interface and some amorphous layers exist at the hetero-interface as shown in the inset of Fig. 1f. Besides, the tCN and $LaPO_4$ are in close contact, forming a 1D heterojunction which cannot be destroyed even after a long time ultrasonication treatment at room temperature. This implies that a solid and extensive interface, rather than a physical mixture, has been formed between the two components, which is very important for the cross-interface electron transfer between the two heterogeneous semiconductors. The chemical bonds formed between them were further studied by X-ray photoelectron spectroscopy (XPS) and Fourier transform infrared (FTIR) analysis. Fig. 1g presents the tentative formation mechanism of the nanocomposites. It has been reported that melamine could be slightly dissolved in ethylene glycol [32], and white melamine precipitation would appear after being protonized by nitric acid. The precipitation was then washed several times by ethanol and dried in an oven followed by calcination at $450^\circ C$. Its surface energy can be reduced by rolling up and forming nanotube structure [32]. However, the pristine tCN suffers from surface defects and structural imperfections because of the incomplete condensation of terminal NH/NH_2 in the repeated units of tri-s-triazine moieties connected by planarized tertiary amino groups [33,34]. In this work, we further calcined the obtained tCN at $550^\circ C$ to elevate its crystallinity and the tubular structure of tCN is well retained after the post-heating treatment (Fig. 1c). Finally, the resultant tCN was dispersed in solution containing La^{3+} and PO_4^{3-} . The anions and cations enter into the tube channels of tCN forced by electrostatic interaction. After hydrothermal treatment, the final $LaPO_4/g-C_3N_4$ samples can be obtained.

The full scan spectrum of XPS analysis is illustrated in Fig. 2a and all the peak positions were calibrated with C 1s peak at 284.6 eV. It indicates that the as conducted La/tCN-200 is composed of C, N, O, La, and P elements. Two peaks with binding energy values of around 854.1 and 835.0 eV can be ascribed to the signals of La $3d_{3/2}$ and $3d_{5/2}$, respectively. Fig. 2b shows that the high resolution spectrum of C 1s can be de-convoluted into two peaks. The one at 284.6 eV is related to the surface adventitious carbon, whereas the other at 288.2 eV confirms the existence of C–N–C coordination

originated from the $g-C_3N_4$ shell [35,36]. It is interesting to find that the intensity of surface adventitious carbon is higher than that of the carbon signal in C–N–C, which may be associated with the tCN synthesis by treating melamine with HNO_3 in the presence of ethylene glycol (EG), where EG will easily polymerize and play an important role in carbonizing and stabilizing the tubular morphology of $g-C_3N_4$. The atomic ratio between C and N of tCN is calculated to be 0.81, which is consistent with the previously reported results [34,37]. To identify the types of nitrogen species, the N 1s peaks of tCN and La/tCN-200 are de-convoluted and presented in Fig. 2c, which show that three peaks at 398.50, 399.44, and 400.40 eV, corresponding to sp^2 hybridized aromatic N bonded to carbon atoms (C=N–C), tertiary N bonded to carbon atoms ($(C)_3-N$) and N–H side groups, are present in both samples [38,39]. Compared with pure $LaPO_4$, the binding energy of La 3d in La/tCN-200 exhibits a positive shift, while P 2p shows a negative shift, suggesting chemical bonding formation between the two components in the composite [40]. FTIR spectroscopy gives a further proof of C–O formation between $LaPO_4$ and $g-C_3N_4$ (Fig. S2). This kind of bonding interaction is essential to the transfer of carriers and thus enhances the photocatalytic activity.

Photo-chemical and photo-electrochemical experiments of the as-prepared samples were performed as depicted in Fig. 3. It is known that tCN has a relatively narrow band gap and much stronger light adsorption than $LaPO_4$. In Fig. 3a, red shifts of the light absorption of La/tCN-x samples can be clearly found, in comparison with that of pure $LaPO_4$. The as-prepared composites show significant light absorption in visible light region, with the absorption edges of La/tCN-100, La/tCN-200, and La/tCN-300 shifted to 331 nm, 424 nm and 450 nm, respectively, which greatly benefits the improvement of their photocatalytic activity [41]. The photoluminescence measurements were also carried out as demonstrated in Fig. 3b. Tubular $g-C_3N_4$ and the composites with high tCN content show broad PL peaks with tails extending to 650 nm. The emission could be ascribed to the band-band PL phenomenon due to the down-transfer of the photoinduced charge carriers in the samples [42]. The peaks at about 440 nm and 470 nm are related to the intrinsic electron transfer (electron-hole recombination) between tCN and $LaPO_4$, which are equivalent to their bandgap energies [43]. $LaPO_4$ sample shows the lowest PL intensity (Fig. 3a) due to its weakest absorption of incident light (Fig. 3b) and smallest amount of photo-generated charge carriers. The emission intensity of the composites increases at the increased dosage of tCN, and the PL quenching is probably due to the charge transfer from tCN to $LaPO_4$. As the amount of tCN increases, the samples' color changes from white to light yellow (demonstrated by their UV–vis absorption spectra in Fig. 3a), which is beneficial to its light absorption enhancement, and subsequently much more electrons can be induced to transfer from tCN to $LaPO_4$ in the nanocomposites. Photoelectrochemical measurements were also carried out to qualitatively study the excitation and transfer of photogenerated charge carriers in the samples. Fig. 3c shows the transient photocurrent responses under intermittent UV–vis illumination for five on-off cycles. It can be clearly seen that a fast and uniform photocurrent response for each switch-on and switch-off run in the three electrodes is present, indicating the extremely fast charge transport in the samples. The tCN presents a quickly increasing current once the light is on and a sharply declining signal with a short delay when the light is off. This kind of transient delay probably stems from the electron trapping and releasing mediated by surface defects [44]. Notably, compared with the two pristine counterparts, the photocurrent density of the La/tCN-200 nanocomposite has been enhanced significantly. Since the photocurrent is mainly produced by the diffusion of photoexcited electrons while the photoexcited holes are captured by hole-acceptor in the electrolyte simultaneously [45], the enhanced photocurrent density of La/tCN-200 means that the photoexcited

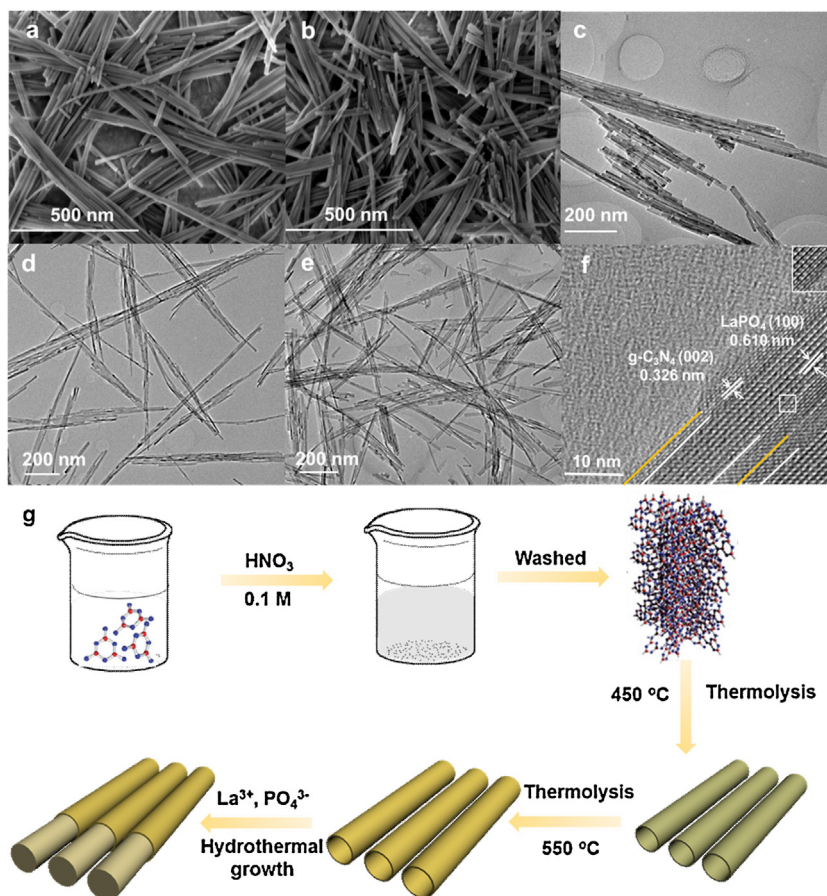


Fig. 1. FE-SEM images of LaPO₄ (a) and La/tCN-200 (b); TEM images of tCN (c), LaPO₄ (d), and La/tCN-200 (e); HRTEM image of La/tCN-200 (f) inserted with the magnified HR-TEM image of the selected area (inset); and schematic illustration of the synthesis of the core-shell LaPO₄/tCN nanocomposites (g).

carriers are separated much more effectively than those in their individuals. To verify this assumption, the charge transfer in dark was studied by electrochemical impedance spectroscopy (EIS) [46]. Only one arc/semicircle can be observed in the frequency ranges on the EIS spectrum as displayed in Fig. 3d, indicating that only surface charge-transfer is involved in the photocatalytic reaction system [47]. The semicircle diameter of La/tCN-200 was much smaller than those of the two individuals, reflecting the efficiently promoted separation of photoinduced electron-hole pairs and the substantially accelerated interfacial charger transfer between the electron donor and acceptor in this heterostructured nanocomposite [48]. These photoelectrochemical results are in good agreement with that of catalytic activity test as will be shown below.

From what has been discussed above, one can safely conclude that compared with the single components, the nanocomposites show excellent light absorption and charge separation. The as-prepared samples were therefore evaluated in detail in an assay of photoreduction of CO₂ at room temperature under ambient pressure. CO was found to be the only carbon-based product of CO₂ reduction and no other carbonaceous signals were detected. Moreover, O₂ was detected in the outlet gases (Fig. S3). Fig. 4a displays the CO evolution on the catalysts and the production rates of CO were in $\mu\text{mol h}^{-1}$. The CO yield over the La/tCN-200 sample reaches 0.433 μmol in the first hour under full-spectrum irradiation, corresponding to 14.43 $\mu\text{mol g}^{-1} \text{h}^{-1}$ on average, which is about 10.36 and 8.07 times as much as those on pure LaPO₄ and tCN, respectively. The hetero-structured photocatalysts usually show significant synergistic effect during the photoreduction reaction [29]. Sample La/tCN-200 exhibits the highest activity for CO₂ reduction among the as-prepared catalysts, which is in line with

the above results of the highest photocurrent density and separation efficiency between electrons and holes. In addition, compared with those nanocomposites in the previous reports, our La/CN-200 nanocomposite performed superior photocatalytic activity for CO₂ reduction under Xenon-light irradiation (Table 1).

As expected, the CO evolution over all the composites are enhanced, while a slight decrease in the production rate takes place upon prolonged irradiation (Fig. S4). The possible reason for this deactivation might be the saturation of the adsorption sites on the catalysts' surface by products and/or intermediates, thus slowing down the subsequent CO₂ reduction [49]. Fig. 4b shows the stability of CO evolution over La/tCN-200 during consecutive runs of 24 h light irradiation. At the end of each run, the sample was collected and treated under 150 °C in an oven for 2 h to eliminate the adsorbed species. No obvious deactivation was observed during the whole test, indicating the excellent photostability of La/tCN-200 sample. In order to investigate its structural stability in the photoreduction of CO₂ with water vapor, the structure of the used composite after a photocatalytic test for 24 h was characterized by XRD analysis (Fig. S5). The results indicate that the structure of the used composite has negligible changes compared with the fresh one, indicating its high structural stability.

The low photocatalytic activity observed on LaPO₄ sample is mainly due to its limited light absorption (Fig. 3), relatively low specific surface area (Fig. S6), and in particular the quick recombination of photogenerated charge pairs. The introduction of tCN into LaPO₄ greatly enhanced its photocatalytic activity for the noble-metal-free CO₂ photoreduction as described above, which cannot be found in previous reports. Such a significant enhancement can be attributed to the light sensitization and band regulation which

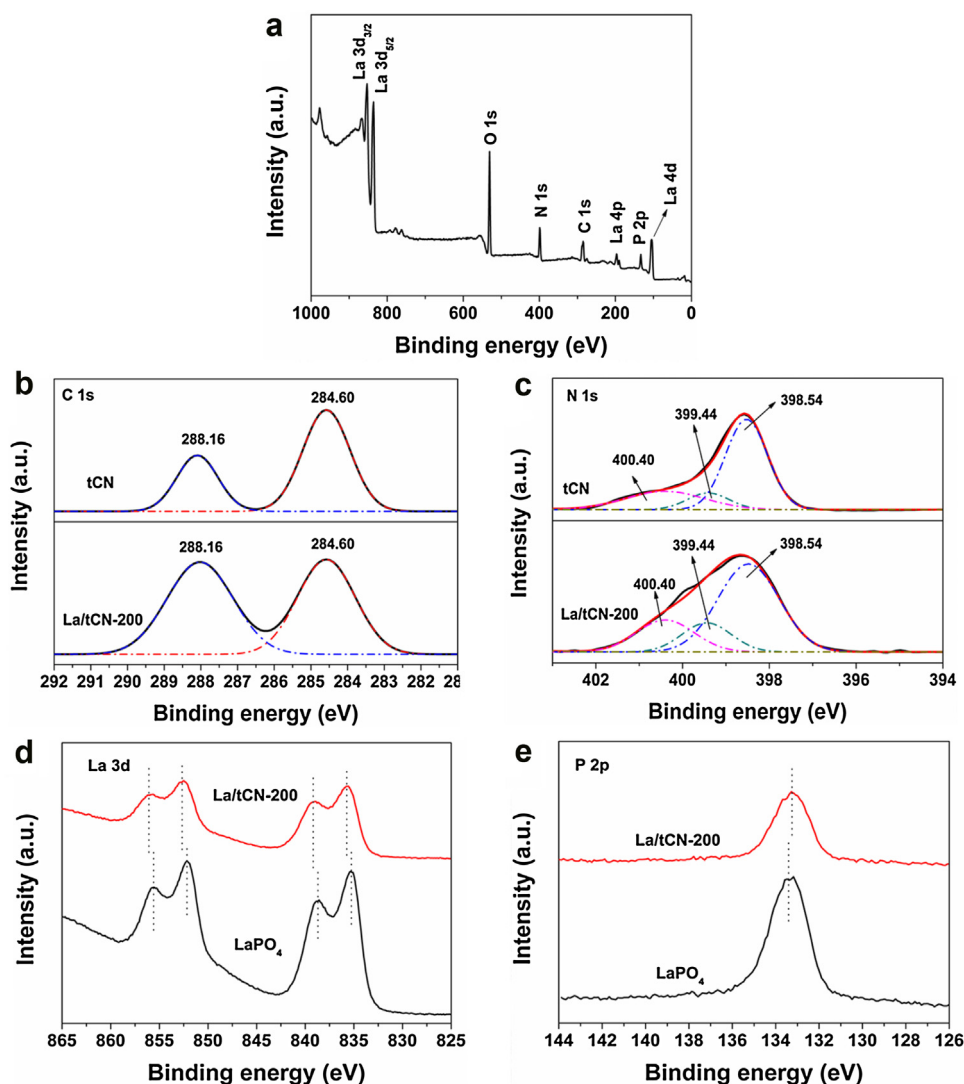


Fig. 2. X-ray photoelectron spectra of La/tCN-200 composite (a), high-resolution spectra of C 1s (b), N 1s (c), La 3d (d), and P 2p (e).

Table 1

Comparison of carbonous evolution rate and photocatalytic activity of the La/tCN-200 nanocomposite with other nanocomposite photocatalysts under Xenon-light irradiation.

Category	System	Co-catalyst	Major product	R_{\max}^a $\mu\text{mol g}^{-1} \text{h}^{-1}$	Minor product	Ref.
$\text{Ti}_{0.92}\text{O}_2/\text{Graphene}$	$\text{CO}_2 + \text{H}_2\text{O}$ (l)	–	CO	8.91	CH_4	[45]
$\text{CeO}_2/\text{g-C}_3\text{N}_4$	$\text{CO}_2 + \text{H}_2\text{O}$ (g)	–	CH_4	13.88	CO, O_2	[13]
$\text{g-C}_3\text{N}_4/\text{KNbO}_3$	$\text{CO}_2 + \text{H}_2\text{O}$ (l)	Pt	CH_4	2.50	–	[46]
$\text{NaNbO}_3/\text{g-C}_3\text{N}_4$	$\text{CO}_2 + \text{H}_2\text{O}$ (l)	Pt	CH_4	6.40	–	[47]
$\text{g-C}_3\text{N}_4/\text{N-graphene}$	NaHCO_3 (0.1 M)	AgBr	CH_4	18.04	CH_3OH , $\text{C}_2\text{H}_5\text{OH}$	[8]
$\text{Bi}_2\text{WO}_6/\text{g-C}_3\text{N}_4$	$\text{CO}_2 + \text{H}_2\text{O}$ (g)	–	CO	5.19	–	[19]
$\text{Cu}_2\text{O}/\text{rGO}$	$\text{CO}_2 + \text{Na}_2\text{SO}_3$ (0.7 M)	–	CO	0.01	–	[48]
$\text{g-C}_3\text{N}_4/\text{N-TiO}_2$	$\text{CO}_2 + \text{H}_2\text{O}$ (g)	–	CO	12.28	CH_4	[49]
$\text{Cu}_2\text{O}/\text{RuO}_x$	$\text{CO}_2 + \text{Na}_2\text{SO}_3$ (0.7 M)	–	CO	0.88	$\text{C}_2\text{H}_5\text{OH}$, CH_4	[50]
$\text{Ce-TiO}_2/\text{SBA-15}$	$\text{CO}_2 + \text{H}_2\text{O}$ (g)	–	CO	1.25	CH_4	[51]
$\text{LaPO}_4/\text{g-C}_3\text{N}_4$	$\text{CO}_2 + \text{H}_2\text{O}$ (g)	–	CO	14.4	O_2	This work

^a R_{\max} Maximum formation rate reported for the major product, in $\mu\text{mol g}^{-1} \text{h}^{-1}$.

results in highly efficient separation/transfer of photogenerated electrons (e^-) and holes (h^+) across the interfaces [50]. Based on above results, a schematic for the superior photocatalytic activity and stability for the nanocomposite is illustrated in Scheme 1.

It is well known that, as a premise for the effective interaction between two components, the band potential matching between them should be ensured during the composite catalyst design and synthesis. As shown in Figs. S7 and S8, the conduction band (CB) and valence band (VB) potentials of tCN are -0.88 and 1.98 eV, while the

CB and VB potentials of LaPO_4 are -0.74 and 3.11 eV, respectively. The more positive CB and VB levels of tCN than those of LaPO_4 mean that a heterojunction between tCN and LaPO_4 will fit the requirements of forming well-matched band structure for photo-induced charge carrier transfer and separation, which will undoubtedly contribute to the enhanced activity of this photocatalyst. In addition to the band potential matching, there are a variety of favorable properties contributing to the high photocatalytic performance of the synthesized composite. First of all, the specific surface area of

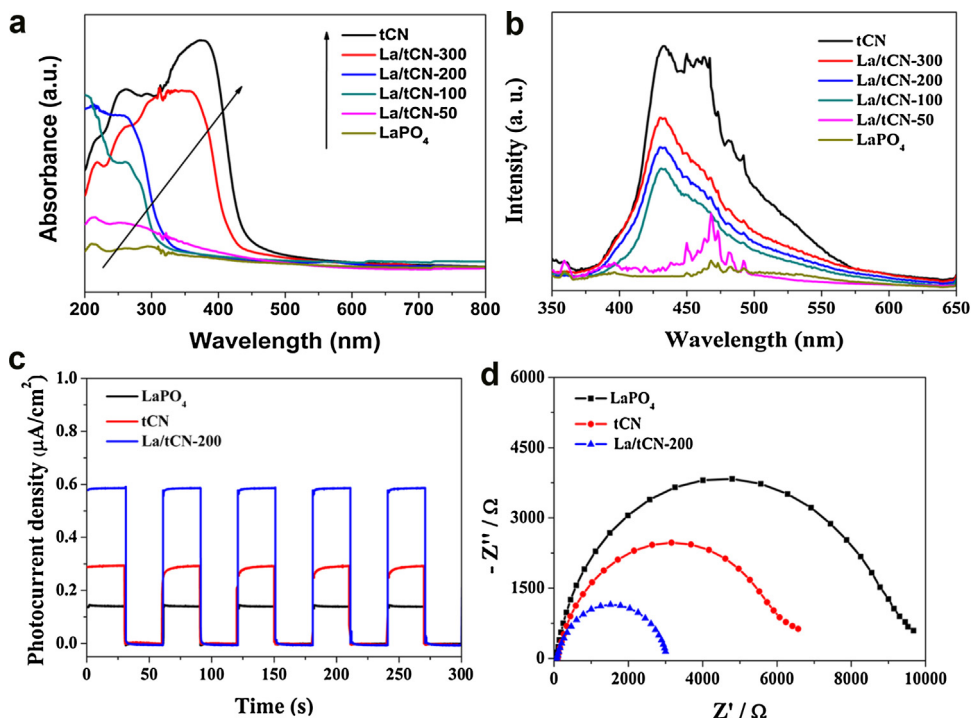


Fig. 3. UV-vis absorption spectra of the as-prepared samples (a), photoluminescence (PL) spectra under 328 nm excitation (b), transient photocurrent density of LaPO₄, tCN, and La/tCN-200 electrodes (c), and EIS Nyquist plots of the samples in dark (d).

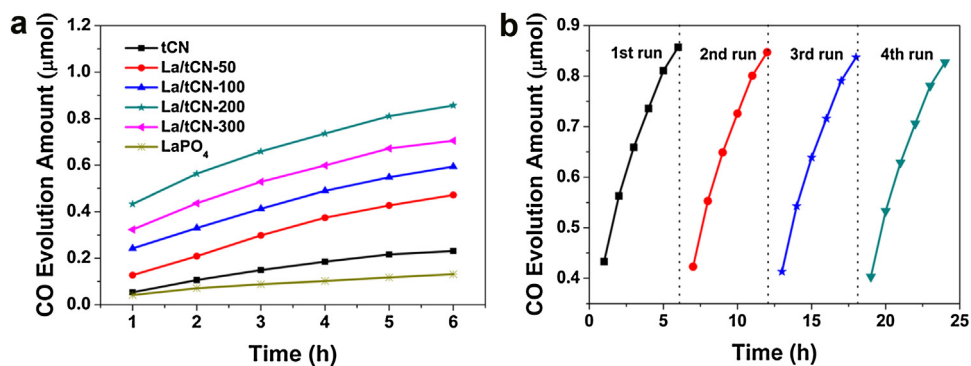
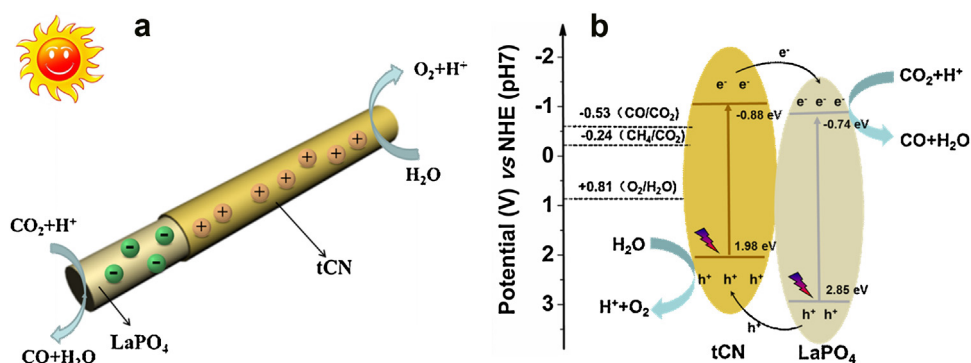


Fig. 4. Time-dependent CO generation over tCN, LaPO₄ and La/tCN composites under full-spectrum irradiation (a). Recycling stability tests over La/tCN-200 (b).



Scheme 1. Schematic illustration of the proposed mechanism in the nanocomposite.

the composite has been enlarged with the addition of tCN, which is beneficial for the effective surface distribution of active sites for CO₂ adsorption and reduction. Secondly, the introduction of tCN will effectively enhance photocurrent response under simulated

sunlight irradiation. More importantly, as indicated by TEM, XPS and FTIR results, the solid and direct contact between tCN and LaPO₄ in the composite enables the highly efficient separation and

transfer of photogenerated charge carriers, resulting in the overall remarkable improvement of its photocatalytic activity.

Once irradiated by simulated sunlight, both tCN and LaPO₄ can produce electrons and holes as illustrated in Scheme 1. Because of the well-matched and overlapping band structure and the extensive interface in close contact, electrons on the CB of tCN will directly transfer to that of LaPO₄, meanwhile, holes on the VB of LaPO₄ transfer to that of tCN spontaneously. This results in an efficient space separation between h⁺ and e⁻, and thus reduces the probability of charge recombination. In this process, both tCN and LaPO₄ are activated. At the VB of tCN, H₂O molecules are oxidized by h⁺, generating O₂ and protons. At the same time, CO₂ molecules can be reduced to CO by e⁻ at the CB of LaPO₄ with the assistance of protons.

4. Conclusions

In summary, a novel 1D LaPO₄/g-C₃N₄ core-shell nanocomposite has been fabricated using a facile hydrothermal method. The photocatalytic CO production capability of the LaPO₄ nanorods is significantly enhanced in the presence of tubular g-C₃N₄ shell, which reaches 0.433 μmol on 30 mg LaPO₄/g-C₃N₄ nanocomposite (La/tCN-200) in the first hour (14.4 μmol g⁻¹ h⁻¹), around 10.36 and 8.07 times that on LaPO₄ and tCN, respectively. More importantly, this core/shell nanocomposite exhibits excellent photostability in the present system. The enhanced photocatalytic activity and photostability may be ascribed to a proposed synergic effect between LaPO₄ and g-C₃N₄ originating from their well-matched band structures, which greatly enhances light sensitivity and effectively accelerates the charge carrier separation/transfer across the bonding interface between tCN and LaPO₄. This novel core/shell structured LaPO₄/g-C₃N₄ nanocomposite without the addition of any noble-metal co-catalyst is a very promising candidate for possible future application in high performance CO₂ photocatalytic reduction and solar fuel production.

Acknowledgements

This work was financially supported by the National Key Basic Research Program of China (2013CB933200), The National High Technology Research and Development Program of China (863 Program, 2012AA062703), National Natural Science Foundation of China (21177137), Youth Innovation Promotion Association CAS (2012200), Shanghai Technical Platform for Testing and Characterization on Inorganic Materials (14DZ2292900) and Jiangsu National Synergetic Innovation Center for Advanced Materials (SICAM).

Appendix A. Supplementary data

Supplementary data associated with this article can be found, in the online version, at <http://dx.doi.org/10.1016/j.apcatb.2016.09.004>.

Notes and references

- [1] A. Dhakshinamoorthy, S. Navalon, A. Corma, H. Garcia, *Energy Environ. Sci.* 5 (2012) 9217–9233.
- [2] A. Kudo, Y. Miseki, *Chem. Soc. Rev.* 38 (2009) 253–278.
- [3] S. Cao, J. Low, Y. Yu, M. Jaroniec, *Adv. Mater.* 27 (2015) 2150–2176.
- [4] X. Dong, F. Cheng, J. Mater. Chem. A 3 (2015) 23642–23652.
- [5] X. Wang, K. Maeda, A. Thomas, K. Takanabe, G. Xin, J. Carlsson, K. Domen, M. Antonietti, *Nat. Mater.* 8 (2009) 76–80.
- [6] P. Tran, L. Wong, J. Barber, J.S.C. Loo, *Energy Environ. Sci.* 5 (2012) 5902–5918.
- [7] W.-J. Ong, L.-L. Tan, S.-P. Chai, S.-T. Yong, *Chem. Commun.* 51 (2015) 858–861.
- [8] K. Wang, Q. Li, B. Liu, B. Cheng, W. Ho, J. Yu, *Appl. Catal. B: Environ.* 176–177 (2015) 44–52.
- [9] H. Li, S. Gan, H. Wang, D. Han, L. Niu, *Adv. Mater.* 27 (2015) 6906–6913.
- [10] Y. Wang, J. Zhang, X. Wang, M. Antonietti, H. Li, *Angew. Chem. Int. Ed.* 49 (2010) 3356–3359.
- [11] Z. Lin, X. Wang, *Angew. Chem. Int. Ed.* 52 (2013) 1735–1738.
- [12] G. Zhang, M. Zhang, X. Ye, X. Qiu, S. Lin, X. Wang, *Adv. Mater.* 26 (2014) 805–809.
- [13] X. Wang, K. Maeda, X. Chen, K. Takanabe, K. Domen, Y. Hou, X. Fu, M. Antonietti, *J. Am. Chem. Soc.* 131 (2009) 1680–1681.
- [14] M. Li, L. Zhang, M. Wu, Y. Du, X. Fan, M. Wang, L. Zhang, Q. Kong, J. Shi, *Nano Energy* 19 (2016) 145–155.
- [15] J. Xu, Y. Wang, Y. Zhu, *Langmuir* 29 (2013) 10566–10572.
- [16] P. Niu, L.-C. Yi, Y.-Q. Yang, G. Liu, H.-M. Cheng, *Adv. Mater.* 26 (2014) 8046–8052.
- [17] F. Cheng, H. Wang, X. Dong, *Chem. Commun.* 51 (2015) 7176–7179.
- [18] X. Fan, L. Zhang, M. Wang, W. Huang, Y. Zhou, M. Li, R. Cheng, J. Shi, *Appl. Catal. B: Environ.* 182 (2016) 68–73.
- [19] S. Chu, Y. Wang, Y. Guo, J. Feng, C. Wang, W. Luo, X. Fan, Z. Zou, *ACS Catal.* 3 (2013) 912–919.
- [20] K. Li, Z. Zeng, L. Yan, S. Luo, X. Luo, M. Huo, Y. Guo, *Appl. Catalysis. B: Environ.* 165 (2014) 428–437.
- [21] M. Li, L. Zhang, X. Fan, Y. Zhou, M. Wu, J. Shi, *J. Mater. Chem. A* 3 (2015) 5189–5196.
- [22] W. Han, A. Zettl, *Adv. Mater.* 14 (2002) 1560–1562.
- [23] Y. Tian, B. Chang, J. Lu, J. Fu, F. Xi, X. Dong, *ACS Appl. Mater. Interface* 5 (2013) 7079–7085.
- [24] B. Pan, Q. Xie, H. Wang, J. Zhu, Y. Zhang, W. Su, X. Wang, *J. Mater. Chem. A* 1 (2013) 6629–6634.
- [25] D. Meziani, A. Rezig, G. Rekhila, B. Bellal, M. Trari, *Energy Convers. Manage.* 82 (2014) 244–249.
- [26] Y. Liu, S. Zhou, J. Li, Y. Wang, G. Jiang, Z. Zhao, B. Liu, X. Gong, A. Duan, J. Liu, Y. Wei, L. Zhang, *Appl. Catal. B: Environ.* 168–169 (2015) 125–131.
- [27] B. Pan, S. Luo, W. Su, X. Wang, *Appl. Catal. B: Environ.* 168–169 (2015) 458–464.
- [28] J. Dai, M. Lv, G. Li, X. Li, *Mater. Design* 83 (2015) 795–800.
- [29] J. Shi, *Chem. Rev.* 113 (2013) 2139–2181.
- [30] H.-D. Xie, F. Li, C. Chen, H.-H. Xi, L. Shi, *J. Inorg. Mater.* 30 (2015) 882–886.
- [31] A. Kar, A. Datta, A. Patra, *J. Mater. Chem.* 20 (2010) 916–922.
- [32] J. Gao, Y. Zhou, Z. Li, S. Yan, N. Wang, Z. Zou, *Nanoscale* 4 (2012) 3687–3692.
- [33] D. Zheng, C. Huang, X. Wang, *Nanoscale* 7 (2015) 465–470.
- [34] J. Sun, J. Zhang, M. Zhang, M. Antonietti, X. Fu, X. Wang, *Nat. Commun.* 3 (2012) 1139–1146.
- [35] M. Tahir, C. Cao, F. Butt, F. Idrees, N. Mahmood, Z. Ali, I. Aslam, M. Tanveer, M. Rizwan, T. Mahmood, *J. Mater. Chem. A* 1 (2013) 13949–13955.
- [36] Y. Zhao, F. Zhao, X. Wang, C. Xu, Z. Zhang, G. Shi, L. Qu, *Angew. Chem. Intern. Ed.* 53 (2014) 13934–13939.
- [37] M. Tahir, N. Mahmood, J. Zhu, A. Mahmood, F. Butt, S. Rizwan, I. Aslam, M. Tanveer, F. Idrees, I. Shakir, C. Cao, Y. Hou, *Sci. Rep.* 5 (2015) 12389–12398.
- [38] C. Zhang, R. Hao, H. Liao, Y. Hou, *Nano Energy* 2 (2013) 88–97.
- [39] S. Wang, C. Li, T. Wang, P. Zhang, A. Li, J. Gong, *J. Mater. Chem. A* 2 (2014) 2885–2890.
- [40] Z. Sun, J. Guo, S. Zhu, L. Mao, J. Ma, D. Zhang, *Nanoscale* 6 (2014) 2186–2193.
- [41] K. Chang, Z. Mei, T. Wang, Q. Kang, S. Ouyang, J. Ye, *ACS Nano* 8 (2014) 7078–7087.
- [42] X. Wang, S. Blechert, M. Antonietti, *ACS Catal.* 2 (2012) 1596–1606.
- [43] H. Yan, H. Yang, *J. Alloy Compd.* 509 (2011) L26–L29.
- [44] D. Jiang, W. Wang, S. Sun, L. Zhang, Y. Zheng, *ACS Catal.* 5 (2015) 613–621.
- [45] S. Meng, X. Ye, X. Ning, M. Xie, X. Fu, S. Chen, *Appl. Catal. B: Environ.* 182 (2016) 356–368.
- [46] H. Fu, T. Xu, S. Zhu, Y. Zhu, *Environ. Sci. Technol.* 42 (2008) 8064–8069.
- [47] Y. Liang, Y. Li, H. Wang, J. Zhou, J. Wang, T. Regier, H. Dai, *Nat. Mater.* 10 (2011) 780–786.
- [48] S. Sun, W. Wang, L. Zhang, *J. Phys. Chem. C* 117 (2013) 9113–9120.
- [49] W.-N. Wang, W.-J. An, B. Ramalingam, S. Mukherjee, D. Niedzwiedzki, S. Gangopadhyay, P. Biswas, *J. Am. Chem. Soc.* 134 (2012) 11276–11281.
- [50] E. Pastor, F. Pesci, A. Reynal, A. Handoko, M. Guo, X. An, A. Cowan, D. Klug, J. Durrant, J. Tang, *Phys. Chem. Chem. Phys.* 16 (2014) 5922–5926.